OPEN ACCESS

Electrochemically Induced Deposition (ECiD) of Lithium Phosphate and the Effect of Reaction Parameters

To cite this article: Ali Amir Saleh *et al* 2026 *ECS Adv.* **5** 013001

View the article online for updates and enhancements.

You may also like

- Nucleation and Growth during Electrochemically Induced Deposition of Li_3PO_4
Ali Amir Saleh, Louis De Taeye, Sai Gourang Patnaik et al.

- Numerical Modelling of Li_3PO_4 Electrochemically Induced Deposition (ECiD) and Determination of True Supersaturation
Ali Amir Saleh, Louis De Taeye, Sai Gourang Patnaik et al.

- The Role of Additives on the Morphology of Li_3PO_4 Film by Electrochemically Induced Deposition (ECiD)
Ali Amir Saleh, Louis De Taeye, Sai Gourang Patnaik et al.

The New PAT-Cell-Solid!

EL-CELL® electrochemical test equipment

Cycle Solid-State Batteries Under Controlled Pressure of up to 300 MPa (6 mm Diameter)!

- Adjust and measure a force of up to 9000 N on the cell stack!
Force adjustment possible throughout the entire experiment
- Built-in force, and temperature sensors!
With optional gas pressure sensor and gas in- and outlet
- PAT-Solid-Core for easy assembly and reproducible results!
Press and cycle solid-state batteries with 6 or 10 mm electrode diameter
- Cableless and highly sealed battery test cell!
For precise long-term measurements of solid-state cell chemistries

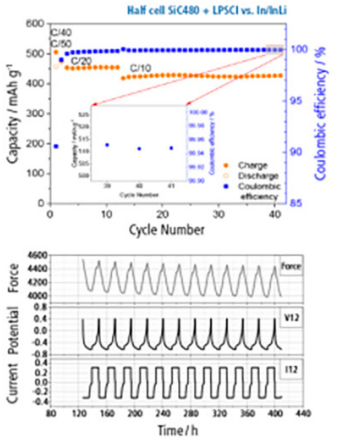

Learn more on our product website: Scan me!

Download the data sheet (PDF): Scan me!

Or contact us directly:

+49 40 79012-734

sales@el-cell.com

www.el-cell.com

This content was downloaded from IP address 134.231.221.187 on 04/06/2026 at 11:12

ECS Advances, 2026 **5** 013001

Electrochemically Induced Deposition (ECiD) of Lithium Phosphate and the Effect of Reaction Parameters

Ali Amir Saleh,[1,2,3,*,z] Louis De Taeye,[2,3] Sai Gourang Patnaik,[2,3] Genis Vanheusden,[2,3] and Philippe Vereecken[2,1,3,,z]**

[1]*KU-Leuven Centre for Membrane Separations, Adsorption, Catalysis, and Spectroscopy for Sustainable Solutions, Leuven 3001, Belgium*
[2]*IMEC, Leuven 3001, Belgium*
[3]*EnergyVille, 3600 Genk, Belgium*

Electrochemically induced deposition (ECiD) is a versatile method for the synthesis of thin films of oxides, phosphates and metal organic frameworks on conductive substrates. The process is based on the electrochemical reaction of a probase, often water electroreduction which generates H_2 and OH^- species, with the latter triggering a deposition reaction in the near-surface diffusion layer. In this work, the ECiD of lithium phosphate was investigated experimentally and by means of numerical modelling. In this system, the electrogenerated OH^- deprotonates phosphate species near the surface and precipitates Li_3PO_4 hemispheres. A growth mechanism is proposed for the ECiD of Li_3PO_4 where surface-adhered H_2 bubbles act as nucleation and growth centers for precipitation. During further growth the subsequently formed H_2 gas escapes via grain boundaries along the radially oriented needle-shaped grains. Hence, the growth process creates its own "chimney" structure. The effect of the reaction parameters on the reaction, specifically the effect of current density, initial phosphate concentration, and bulk pH were investigated and used to validate the model. The addition of ethanol as co-solvent and surfactant, and cetyltrimethylammonium bromide (CTAB) as surfactant and micellular species, was shown to affect morphology greatly. Strategies for optimizing the parameters towards desired morphologies are discussed.
© 2026 The Author(s). Published on behalf of The Electrochemical Society by IOP Publishing Limited. This is an open access article distributed under the terms of the Creative Commons Attribution 4.0 License (CC BY, https://creativecommons.org/licenses/by/4.0/), which permits unrestricted reuse of the work in any medium, provided the original work is properly cited. [DOI: 10.1149/2754-2734/ae3780]

Manuscript submitted November 25, 2025; revised manuscript received January 9, 2026. Published January 22, 2026.

Supplementary material for this article is available online

Electrochemically induced deposition (ECiD) is a technique in which an electrochemical reaction triggers a subsequent deposition reaction. This is generally achieved by the electrochemical reduction or oxidation of a probase. The product of the electrochemical probase redox reaction accumulates near the electrode surface in what is known as the diffusion layer and its change in concentration triggers a deposition reaction. This probase is commonly water, protons, or nitrate but can in principle be anything that undergoes a redox reaction and produces a reaction product that triggers the targeted deposition reaction.[1] ECiD, also referred to as the "generation of base method," has previously been utilized to coat electrode surfaces with metal oxides, metal hydroxides, and metal phosphates.[2–7] One specific example is the ECiD of hydroxyapatite (HAp) with chemical composition $Ca_5(PO_4)_3(OH)$. Since calcium phosphates makes up 60% of bone density and 90% of tooth enamel, their derivatives have been used for applications in bone regeneration and osseointegration.[8] HAp in particular has been utilized for these applications since the late 1960s due to its chemical stability and excellent biocompatibility.[7] In the ECiD of HAp water is used as the probase. At potentials where the hydrogen evolution reaction occurs, water is reduced and produces OH^- ions Eq. 1.1).[6] The generated OH^- accumulates near the electrode surface in the diffusion layer.[9] This causes the local pH to increase as a response to the water equilibrium (Eq. 1.2).

$$2H_2O \rightleftharpoons 2OH^- + H_2 \quad U = 0.83\ V - 0.0592\ pH \qquad [1.1]$$

$$H_2O \underset{k_{bw}}{\overset{k_{fw}}{\rightleftharpoons}} H^+ + OH^- \quad K_w = [OH^-][H^+] = 1 \times 10^{-14}\ M^2 \qquad [1.2]$$

The increase in local pH triggers the deprotonation of phosphoric acid (H_3PO_4) to phosphate monobasic ($H_2PO_4^-$) ($pK_a = 2.12$) (Eq. 1.3), the deprotonation of phosphate monobasic to phosphate dibasic (HPO_4^{2-}) ($pK_a = 7.21$) (Eq. 1.4), and the deprotonation of phosphate dibasic to phosphate tribasic (PO_4^{3-}) ($pK_a = 12.7$) (Eq. 1.5).[9]

$$H_3PO_4 + OH^- \underset{k_{b1}}{\overset{k_{f1}}{\rightleftharpoons}} H_2PO_4^- \quad K_{b1} = \frac{[H_2PO_4^-]}{[H_3PO_4][OH^-]} = 7.52 \times 10^{11}\frac{1}{M} \qquad [1.3]$$

$$H_2PO_4^- + OH^- \underset{k_{b2}}{\overset{k_{f2}}{\rightleftharpoons}} HPO_4^{2-} \quad K_{b2} = \frac{[HPO_4^{2-}]}{[H_2PO_4^-][OH^-]} = 6.23 \times 10^{6}\frac{1}{M} \qquad [1.4]$$

$$HPO_4^{2-} + OH^- \underset{k_{b3}}{\overset{k_{f3}}{\rightleftharpoons}} PO_4^{3-} \quad K_{b3} = \frac{[PO_4^{3-}]}{[HPO_4^{2-}][OH^-]} = 4.8 \times 10^{1}\frac{1}{M} \qquad [1.5]$$

In the presence of calcium ions (Ca^{2+}), phosphate tribasic (PO_4^{3-}) reacts with Ca^{2+} and OH^- and HAp precipitates (Eq. 1.6) and coats the electrode surface.

$$5Ca^{2+} + 2PO_4^{3-} + OH^- \rightleftharpoons Ca_5(PO_4)_3(OH) \qquad [1.6]$$

The resulting HAp coating consists of dispersed particles coalesced into a closed layer with high surface area. This makes the coating suitable for applications as biocompatible coatings for medical implants as it contains a large surface area in which tissue can grow and anker the implant.[8] This morphological control was enabled by the investigation and understanding of the reaction mechanism, providing knowledge on how to best optimize and control the reaction parameters towards yielding the desired coating properties. Another example of ECiD is the lithium phosphate (Li_3PO_4) system.[10,11] Li_3PO_4 has applications as a thin-film solid

*Electrochemical Society Student Member.
**Electrochemical Society Member.
[z]E-mail: ali.saleh@kuleuven.be; philippe.vereecken@imec.be

electrolyte (SE) in thin-film solid-state batteries (TFSSBs) or as a thin artificial solid electrolyte interface (ASEI) coating on lithium metal anodes.[12] A thin-film SE and an ASEI coating must be as thin and as uniform as possible to maximize ion conductivity uniformly across the interface and mechanically stable enough to withstand the great pressure exerted on it by lithium dendrites.[12] The ion conductivity of Li_3PO_4 is sufficient for these tasks if kept a few tens to a couple hundred nm thin, while its stress resistance makes it capable of suppressing dendrite formation.[12] Like in the ECiD of HAp, water reduction produces an elevated OH^- concentration near the electrode surface, which triggers the deprotonation of phosphate ions in solution. In the presence of Li^+ ions, Li_3PO_4 precipitates and coats the electrode surface (Eq. 1.7).[10,11]

$$3Li^+ + PO_4^{3-} \rightleftharpoons Li_3PO_4 \qquad K_{sp} = [Li^+]^3[PO_4^{3-}] = 2.37 \times 10^{11} \qquad [1.7]$$

The resulting coating consists of dispersed particles coalesced into a nonuniform closed layer with a high degree of pinhole-like porosity. This is not suitable for the intended applications as thin-film SE or thin ASEI. Therefore, significant optimization of the Li_3PO_4 coating morphology is needed before it can be relevant for TFSSBs. In contrast with the ECiD of HAp, the ECiD of Li_3PO_4 has not been investigated and its mechanism is largely unknown. Therefore, there is no clear indication from the literature as to how to manipulate the reaction parameters to obtain the desired uniform and pinhole-free coatings. Direct knowledge transfer from the ECiD of HAp is also not perfect as the desired HAp coating properties are fundamentally different from those desired for Li_3PO_4.

The goal of this work is therefore to understand the effect of the Li_3PO_4 reaction parameters on the morphology of the produced deposit. This was done by combination of numerical model and experimental validation. The numerical model was used for speciation and to determine the concentration and pH profiles in the diffusion layer for different reaction parameters, namely reaction time, current density, bulk pH, and initial phosphate concentration, $[H_2PO_4^-]_0$. This provided insight into the thermodynamic driving force of the reaction for different reaction conditions and guided the optimization of the reaction parameters. The effect the reaction parameters have on morphology was studied systematically and correlated to surface concentration profiles obtained from the model. In addition to the forementioned reaction parameters, the effect of solvent composition and additives was investigated.

Methods

Electrochemically induced deposition experiments.—The different precursor solutions used for these experiments can be found in Table I below.

The chemicals used are LiH_2PO_4 (99% Sigma-Aldrich), Li_2SO_4 (99.5% Sigma-Aldrich), ethanol absolute (VWR chemicals), and cetyltrimethylammonium bromide (CTAB) (99% Sigma-Aldrich). Electrochemical induced deposition was performed under galvanostatic conditions from solutions A-E. A 3-electrode PTFE cell (Fig. SI.A1) was used with a Si/10 nmTi/150 nmTiN wafer coupon as the stationary working electrode with an exposed area of 0.622 cm^2 (as defined by an O-ring), Ti gauze counter electrode (GoodFellow, 60 wires/inch mesh, 0.23 mm diameter wires), and an Ag/AgCl in 3 M KCl reference electrode, placed in a separate compartment connected by a Luggin capillary. Electrochemical conditions were applied and monitored by a Metrohm Autolab PGSTAT30 potentiostat with a Nova 1.11 software. After deposition, the samples were rinsed with rinsed with D.I. water by gentle flow from a 2 mL dropper and subsequently dried carefully in a stream of N_2 gas from a N_2 gun.

Numerical model.—A steady-state diffusion model was implemented where the speciation in a diffusion layer of thickness δ was calculated vs time t and distance x from the electrode surface according to the equations in the Supporting Information appendix B (SI.B). A boundary layer thickness of 500 μm was set in the model such that the entirety of the diffusion layer can be modelled within the time constrains considered. A boundary condition of concentration of species i, c_i, equals that of the bulk concentration c_{bulk} ($c_i(x = 500, t) = c_{bulk}$), was applied at the bulk end of the boundary layer. The diffusion coefficients, equilibrium constants, and rate constants were obtained from literature and can also be found in SI. B. The equations were solved by utilizing COMSOL Multiphysics® 6.1.

Characterization.—The sample morphologies were characterized and their dimensions analyzed qualitatively and quantitatively by scanning electron microscopy (SEM) (Phillips XL30). The chemical composition of the synthesized samples was characterized by attenuated total reflectance (ATR) Fourier transform infrared spectroscopy (FTIR) (Bruker 5 FTIR) with a diamond ATR crystal and with an OPUS 5.0 software. The elemental ratios of the samples were characterized by means of a Time-of-flight energy elastic recoil detection analysis (ERDA) with a $^{35}Cl^{4+}$ (8 MeV) primary beam with a scattering angle of 40° and a sample tilt of 20°. X-ray diffraction (XRD) analysis was performed by a Rigaku SmartLab X-ray diffractometer with a CuKα1 (1.541 Å) radiation source and operated via a SmartLab Studio II software.

Results and Discussion

In the ECiD of lithium phosphate, the precipitation of Li_3PO_4 on the electrode surface is governed by the local pH near the electrode surface. To gain insight into how to leverage the reaction parameters towards the desired coating properties, numerical modelling and experimental investigations of the ECiD process and its reaction parameters were performed. In a first step, the surface pH profiles were determined numerically using Finite Element Modeling. Water is used as the probase, i.e. the water is electrochemically reduced to H_2 with the formed OH^- biproduct accumulating in the diffusion layer causing an elevated near-surface pH. The model calculated the flux of OH^- generated by hydrogen evolution reaction (HER) (Eqs. 1.1 and 1.2) under galvanostatic conditions (the condition used experimentally) on a stationary metal electrode. This was done by solving the Nernst-Planck equation (excluding convection and migration) (Eq. 3.1);

$$J_{OH^-}(x) = -D_{OH^-}\frac{\partial[OH^-](x, t)}{\partial x} \qquad [3.1]$$

Table I. Composition of each solution used in this work.

Solution	$[Li_2SO_4]$ (M)	$[LiH_2PO_4]$ (M)	Solvent	[CTAB] (M)	Solution pH
Solution A	1.5	0.5	H_2O	None	3.8
Solution B	1.5	0.5	H_2O	None	2.5
Solution C	1.5	0.5	H_2O	None	4.5
Solution D	1.5	0.1	H_2O	None	3.8
Solution E	1.5	0.5	15 v/v% ethanol	None	4.0
Solution F	1.5	0.5	15 v/v% ethanol	0.075	4.0

with $J_{OH^-}(x)$ being the flux of OH^- ions with respect to distance x from the electrode surface, D_{OH^-} being the diffusion coefficient of OH^- ions in solution, and $\frac{\partial[OH^-](x,t)}{\partial x}$ as the change in OH^- concentration with respect to distance x from the electrode surface. Equation 3.1 allows the calculation of the concentration of OH^- at each point in the diffusion layer. At the electrode surface where x = 0 and the HER occurs, the flux of OH- ions is controlled by the current density applied, and Eq. 3.1 can be rewritten;

$$J_{OH^-}(x=0) = -\frac{i}{nF} = -D_{OH^-}\frac{\partial[OH^-](x,t)}{\partial x} \quad [3.2]$$

where $J_{OH^-}(x=0)$ is the flux of OH^- ions at the electrode surface, i is the current density, n is the number of electrons exchanged in the HER, and F is the Faraday constant. This allows us to directly relate the applied current to the flux of OH^- at the electrode surface. The actual local OH^- concentration, however, will adjust due to the local buffering effect of phosphate compounds described by the acid-base equilibria of reactions Eqs. 1.3 to 1.5 leading to the modified equation of Fick's 2nd law (Eq. 3.3),

$$\frac{\partial[OH^-](x,t)}{\partial t} = -D_{OH^-}\frac{\partial^2[OH^-(x,t)]}{\partial x^2} + r_{OH^-} \quad [3.3]$$

with r_{OH^-} is the rate of OH^- consumption or formation and given by:

$$\begin{aligned} r_{OH^-} = &-(k_{f,w}[H^+][OH^-] - k_{b,w}K_w) \\ &+ (k_{b1}[H_2PO_4^-] - k_{f1}[OH^-][H_3PO_4]) \\ &+ (k_{b2}[HPO_4^{2-}] - k_{f2}[OH^-][H_2PO_4^-]) \\ &+ (k_{b3}[PO_4^{3-}] - k_{f3}[OH^-][HPO_4^{2-}]) \\ &+ (k_{b5}[HSO_4^-] - k_{f5}[OH^-][H_2SO_4]) \\ &+ (k_{b6}[SO_4^{2-}] - k_{f6}[OH^-][HSO_4^-]) \end{aligned} \quad [3.4]$$

As Li_2SO_4 was added next to LiH_2PO_4 also the acid-base equilibria for sulphate species were taken into account:

$$H_2SO_4 + OH^- \underset{k_{b5}}{\overset{k_{f5}}{\rightleftharpoons}} HSO_4^- \quad K_{b5} = \frac{[HSO_4^-]}{[H_2SO_4][OH^-]} = 1.2\times10^{15}\frac{1}{M} \quad [3.5]$$

$$HSO_4^- + OH^- \underset{k_{b6}}{\overset{k_{f6}}{\rightleftharpoons}} SO_4^{2-} \quad K_{b6} = \frac{[SO_4^{2-}]}{[HSO_4^-][OH^-]} = 1.2\times10^{12}\frac{1}{M} \quad [3.6]$$

The rate of OH^- consumption depends on the water equilibrium, K_w, and the phosphoric acid and sulfuric acid deprotonation reactions with forward reaction rate constants, k_{f1}, k_{f2}, k_{f3}, k_{f5}, k_{f6}, while the rate of OH^- formation depends on the protonation reactions with backward reaction rate constants, k_{b1}, k_{b2}, k_{b3}, k_{b4}, k_{b1}, The assumption was made that all the forward and backward reaction rates are sufficiently fast such that the acid-base reactions universally reach instantaneous equilibrium with any finite perturbation. Literature values were used for diffusion coefficients and backward rate constants k_{bi}[13–15] and are given in SI.B. Forward rate constants for species i, k_{fi}, were calculated from $K_i = k_{fi}/k_{bi}$. Similar equations to Eq. 3.3 were derived to obtain time and distance dependent equations for the concentrations of each species in solution. Here, the equation for the rate of PO_4^{3-} formation is given Eq. 3.7, for the other species we refer to the SI.B.

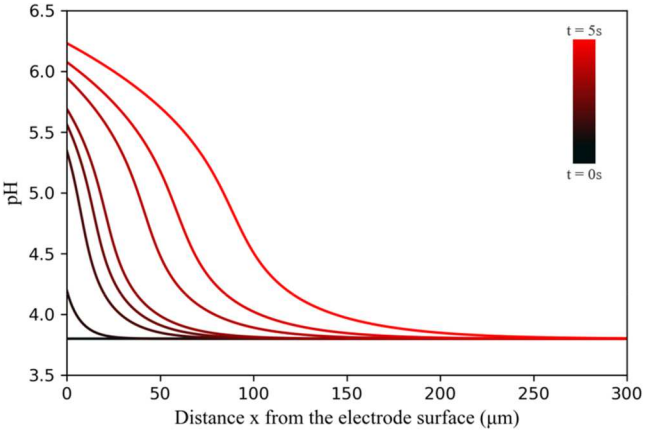

Figure 1. pH profile in the diffusion layer established after 5 s of HER in solution A (an aqueous solution of 0.5 M LiH_2PO_4 and 1.5 M Li_2SO_4 with a bulk pH of 3.8) by a cathodic current density of −6.3 mA cm^{-2}.

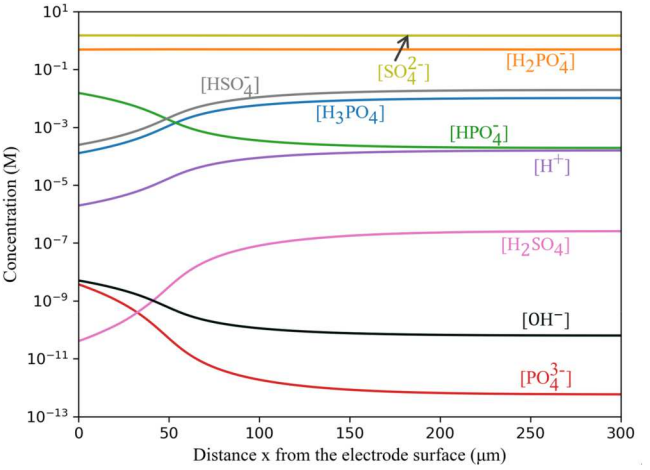

Figure 2. Numerical model of the complete speciation profile in the diffusion layer after 5 s of the reaction using solution A (an aqueous solution of 0.5 M LiH_2PO_4 and 1.5 M Li_2SO_4 with a bulk pH of 3.8) with a current density of −6.3 mA cm^{-2}, where concentration, given in Molar, is plotted against distance x from the electrode, given in μm.

$$\frac{\partial[PO_4^{3-}](x,t)}{\partial t} = D_{PO_4^{3-}}\frac{\partial^2[PO_4^{3-}](x,t)}{\partial x^2} + r_{PO_4^{3-}} \quad [3.7]$$

Figure 1 shows the pH profile evolution calculated for an aqueous solution comprising 0.5 M LiH_2PO_4 and 1.5 M Li_2SO_4 (Solution A). At the start of the hypothetical experiment, before a current is applied, the pH is 3.8 throughout the electrolyte. Upon application of a cathodic current ($i = -6.3$ mA cm^{-2}), the local pH near the electrode surface increases quickly as a response to the formation of the diffusion layer, driven by HER. Interestingly, after 5 seconds, the surface pH stabilizes at a value of 6.3, indicating that the formed OH^- is consumed by other species than water and that it doesn't contribute to raising the surface pH anymore.

Figure 2 shows the diffusion layer speciation profile at t = 5 s. It shows the prevalence of the completely deprotonated sulphate dibasic (SO_4^{2-}) and the phosphate monobasic species ($H_2PO_4^-$) in the bulk with concentrations of nearly 1.5 M and 0.5 M, respectively. They are followed by sulphate monobasic (HSO_4^-) and the completely protonated phosphoric acid (H_3PO_4) both with

concentrations in the order of 10^{-2} M, and phosphate dibasic (HPO_4^{2-}) with a concentration of 10^{-4} M. These four species (SO_4^{2-} excluded) are all capable of undergoing a deprotonation reaction by reacting with OH^- ion in solution as is made clear from equations Eqs. 1.3 to 1.5 and Eqs. 3.4 to 3.6, thus all contribute to buffering the solution pH. Furthermore, the concentrations of these species change near the electrode surface when a cathodic current is applied. While the HSO_4^- and H_3PO_4 concentrations decrease from 10^{-2} M to 10^{-4} M, the HPO_4^{2-} and PO_4^{3-} concentrations increase from 10^{-4} M to 10^{-2} M and 10^{-13} M to nearly 10^{-8} M, respectively. This indicates that H_3PO_4 is reacting to form $H_2PO_4^-$, HPO_4^{2-}, and PO_4^{3-}, while HSO_4^- is reacting to form SO_4^{2-}. The dominant phosphate species near the surface remains $H_2PO_4^-$ and its concentration is constant during its buffering action (governed by Eq. 1.4) and is the primary reason for stagnating surface pH (pH_s) at 6.3 in Fig. 1. However, the deprotonation of HSO_4^-, H_3PO_4, and HPO_4^{2-} (governed by Eqs. 3.6, 1.3, and 1.5, respectively) result in non-negligible buffering of the surface pH and must therefore be taken into account. Effectively this means that as water is reduced near the electrode surface and OH^- is produced, a large part of it is consumed in the deprotonation of the hydrogenated phosphate and sulphate species and the solution pH is buffered. Note that in pure water, the surface pH would quickly surpass 10 even for current densities as low as -0.1 mA cm^{-2} (see example in SI.C1). Also note that the dynamics of electroformed H_2 gas likely influences local convection and limits the accuracy of the modelled diffusion layer but is too complex to incorporate into the numerical model without relying on many assumptions. Furthermore, the numerical model merely identifies trends, thus the implementation of the effect of bubble dynamics would not result in significant added value.

Further, Fig. 2 show an increase of $[PO_4^{3-}]$ by 4 orders of magnitude. In the presence of the 3.5 M Li^+ ions, this leads to the precipitation of Li_3PO_4 in the near surface region as the activity of PO_4^{3-} and Li^+ exceeds the solubility product of Li_3PO_4 (Eq. 1.7). When the precipitation reaction is confined close to the electrode surface, the electrode is expected to be coated with a layer of Li_3PO_4. While PO_4^{3-} is the dominant anion in the Li_3PO_4 precipitation reaction, the role of $H_2PO_4^-$ and HPO_4^{2-} in influencing crystal shapes and morphology cannot be ruled out.

Next, galvanostatic ECiD experiments were performed on TiN substrates at -6.3 mA cm^{-2} from an aqueous solution of 0.5 M LiH_2PO_4 and 1.5 M Li_2SO_4 (Solution A). Figures 3a–3e show SEM images of deposits obtained after different durations, while Fig. 3f shows the corresponding potential transients. As predicted, a lithium phosphate deposit was formed on the electrode surface after some time and the amount of deposit increases with time. After 40 seconds of deposition (Fig. 3a, a distribution of small particles ($\sim$60 nm, 2×10^7 particles cm^{-2}) was formed on the electrode surface. Note that around the edges of the sample, where gas bubbles easily accumulate and local ion concentration gradients differ from the center, a ring of thicker deposit was seen which formed already at shorter times (Fig. SI.C2a). Edge effects are common features in electrodepositions and are industrially addressed by, among other approaches, shields to regulate the current distribution. After 280 seconds the deposits have increased in size (exceeding 2 μm) while new ones have formed in between (Fig. 3b); i.e., following progressive nucleation and growth modus. As the particles grow, their shapes become more spherical. After 350 seconds, the surface coverage has further increased, and particles have grown even larger in size forming clusters (Fig. 3c). After 600 s (Fig. 3d, a closed layer is formed where gaps between spherical particles have been filled in. The coating consists of $\sim$5 μm high large hemispherical particles with an interconnecting layer of not more than 1 μm in thickness (Figs. 4 and SI.C5). The point where the film closes (after 600 s in this case) corresponds to a minimum in the transient. This is henceforth referred to as the point of maximum coverage. After longer deposition (in this case 750 seconds), the films were found to crack and delaminate as shown in Fig. 3e. From the SEM cross-section, a 10 μm layered deposit can be seen.

The potential transients hold information about the progress of deposition by precipitation reaction. The only electrochemical reaction throughout the deposition process is the HER. However, as the surface is progressively covered by Li_3PO_4, which is electronically insulating, the local or effective current density increases as the exposed TiN electrode surface decreases. Hence, the overpotential for HER must increase to maintain the same applied current. In the first part of the deposition reaction, the U-t transient in Fig. 3f shows the potential becomes more positive from around -1.5 V to around -1.3 V. This region spans the first 220 s, which suggests that this change in potential corresponds to the formation of the initial deposits on the electrode surface (Figs. 3a and 3b). The effect of surface coverage increase is most clearly seen between 217 s and 600 s in Fig. 3f. After 217 s the potential becomes steadily more negative until 600 s, or the point of maximum coverage. Once full surface coverage is obtained, the potential levels off and reaches a plateau (after 600 s until 750 s in this case). In the plateau region, at even longer times (Fig. SI.C4). The potential seems to oscillate somewhat, and the plateau slopes positively in potential, consistent with a multilayered and poorly adhering morphology observed after rinsing and drying in Fig. 3e. Note that an oscillating and at times noisy potential trace was present throughout all measurements and could be indicative of a changing concentration gradient and precipitation reaction kinetics.

Figures 4a and 4b provide a closer look at the particles at the point of maximum coverage (at 600 s) i.e., when the spaces are filled in between the particles as described above with Fig. 3d. The particles are hemispherical in shape and, interestingly, contain a cavity in the center. Furthermore, the thick shell is porous and built out of primary needle-like structures arranged in a radial fashion around the cave. Additionally, this shell appears to consist of multiple layers or subshells as is evident in Fig. 4b. As for the layers in Fig. 4b and discussion of oscillatory transient behavior, these subshells indicate the process of precipitation is non-continuous. It is postulated here that the cavity inside the hemispherical particle is the remnant of small H_2 bubbles formed and adhered to the surface during initial stages of current flow for HER. The hydrogen bubbles then likely serve as nucleation and coalescence sites for these primary Li_3PO_4 particles. The reaction proceeds as hydrogen gas can escape or diffuse through the narrow pores in-between the needles and guiding the needle formation.

Thus far, a general description of the ECiD of Li_3PO_4 was given for one specific condition (Solution A and $i = -6.3$ mA cm^{-2}). Figure 5 shows outputs of the numerical models for different current densities, bulk pH, and initial phosphate monobasic concentrations ($[H_2PO_4^-]_0$) showing their effect on the surface and the near surface pH and $[PO_4^{3-}]$. Increasing the cathodic current density (Fig. 5a) from -1.3 mA cm^{-2} to -18.9 mA cm^{-2} results in a more alkaline pH near the electrode surface (pH_s from 4.6 to 6.9, respectively) and a higher surface $[PO_4^{3-}]$ (from 3×10^{-11} M to 6×10^{-7} M, respectively). This suggests that the precipitation reaction would be faster with a higher applied cathodic current density. An increase in bulk pH from 2.5 to 4.5 (Fig. 5b) results in a more alkaline surface pH (from 2.7 to 6.3, respectively) and higher surface $[PO_4^{3-}]$ (from 3×10^{-15} M to 6×10^{-8} M, respectively). This suggests a larger driving force towards precipitation when a larger bulk pH is used. It is worth noting that a change in bulk pH between 3.8 to 4.5 results only in a marginal change in surface pH (surface pH from 6.2 to 6.3, respectively) and in $[PO_4^{3-}]$ (from 4×10^{-8} M to 6×10^{-8} M, respectively), as the phosphate buffering is effective in this pH range (pKa = 7.21 for reaction in Eq. 1.4). Figure 5c shows that the $[H_2PO_4^-]_0$ has a large effect on both the surface pH and $[PO_4^{3-}]$. The surface pH is more alkaline for lower $[H_2PO_4^-]_0$ (6.2 to 7.3 for 0.5 M and 0.1 M, respectively) and the $[PO_4^{3-}]$ is one order of magnitude greater near the electrode surface (4×10^{-8} M to 5×10^{-7} M, respectively). This suggests a larger driving force towards precipitation when larger initial phosphate monobasic is used. Note that this effect on surface pH and $[PO_4^{3-}]$ is far greater than what is calculated for a changing current density or bulk pH,

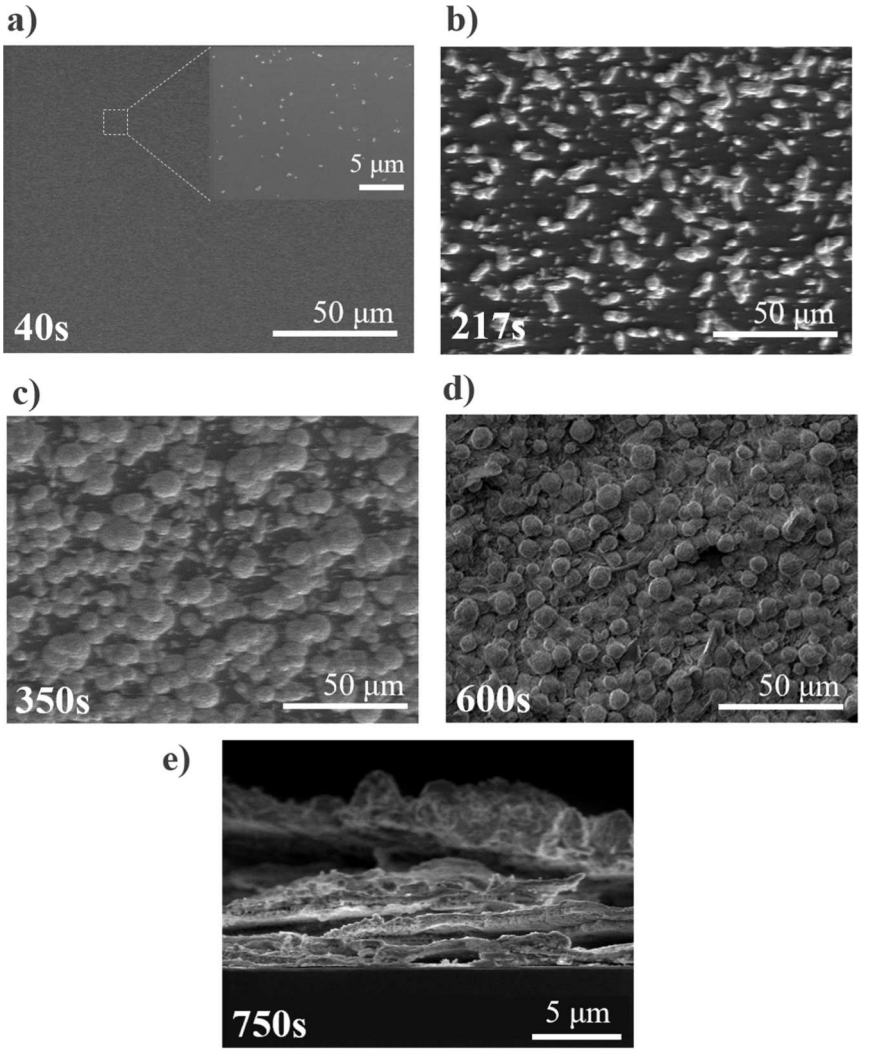

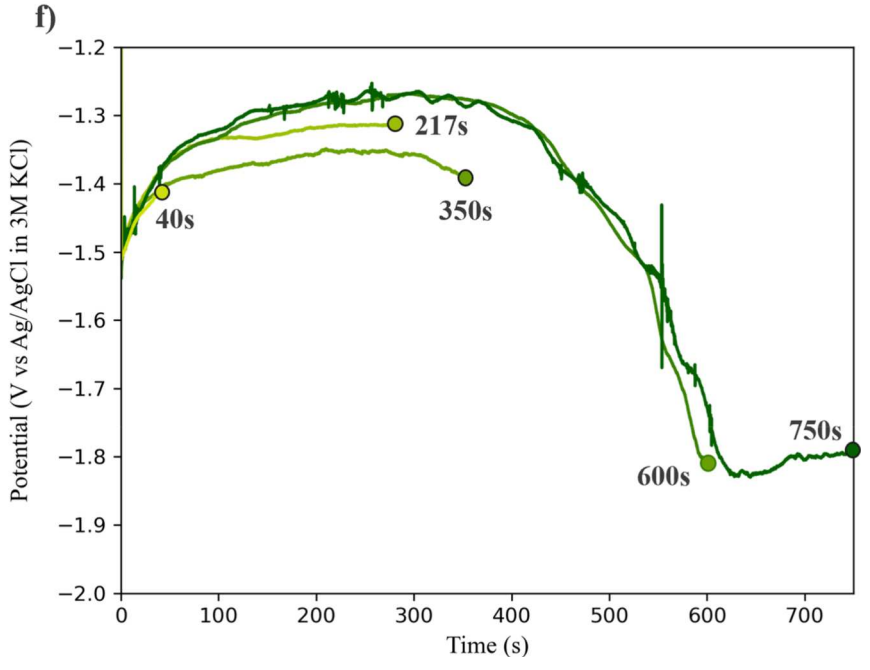

Figure 3. This figure displays a-e) the SEM top view at the first 4 stages and a cross-section view at the last stage of a deposition from a galvanostatic reaction performed using solution A (an aqueous solution of 0.5 M LiH_2PO_4 and 1.5 M Li_2SO_4 with a bulk pH of 3.8) with $i = -6.3$ mA cm^{-2} on a TiN substrate, and f) the U-t transient for a galvanostatic reaction performed using solution A with $i = -6.3$ mA cm^{-2}, with Potential, given in V vs Ag/AgCl in 3 M KCl, plotted against time, given in seconds.

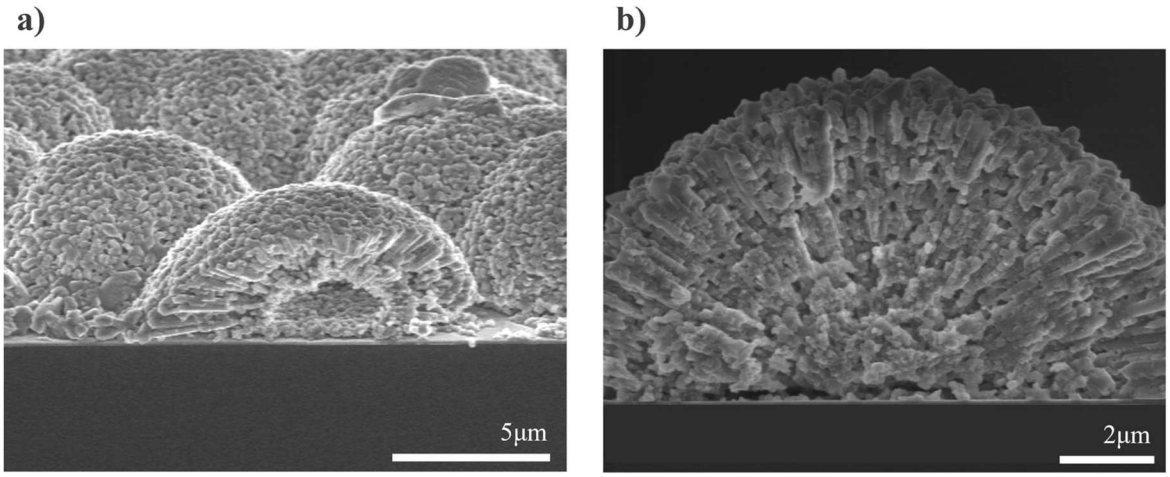

Figure 4. This figure displays (a) an SEM image of a 25° tilted view, and (b) an SEM image of a cross-section view of a typical deposit morphology from a galvanostatic reaction performed with solution A (an aqueous solution of 0.5 M LiH_2PO_4 and 1.5 M Li_2SO_4 with a bulk pH of 3.8) and an applied current density of -6.3 mA cm^{-2}.

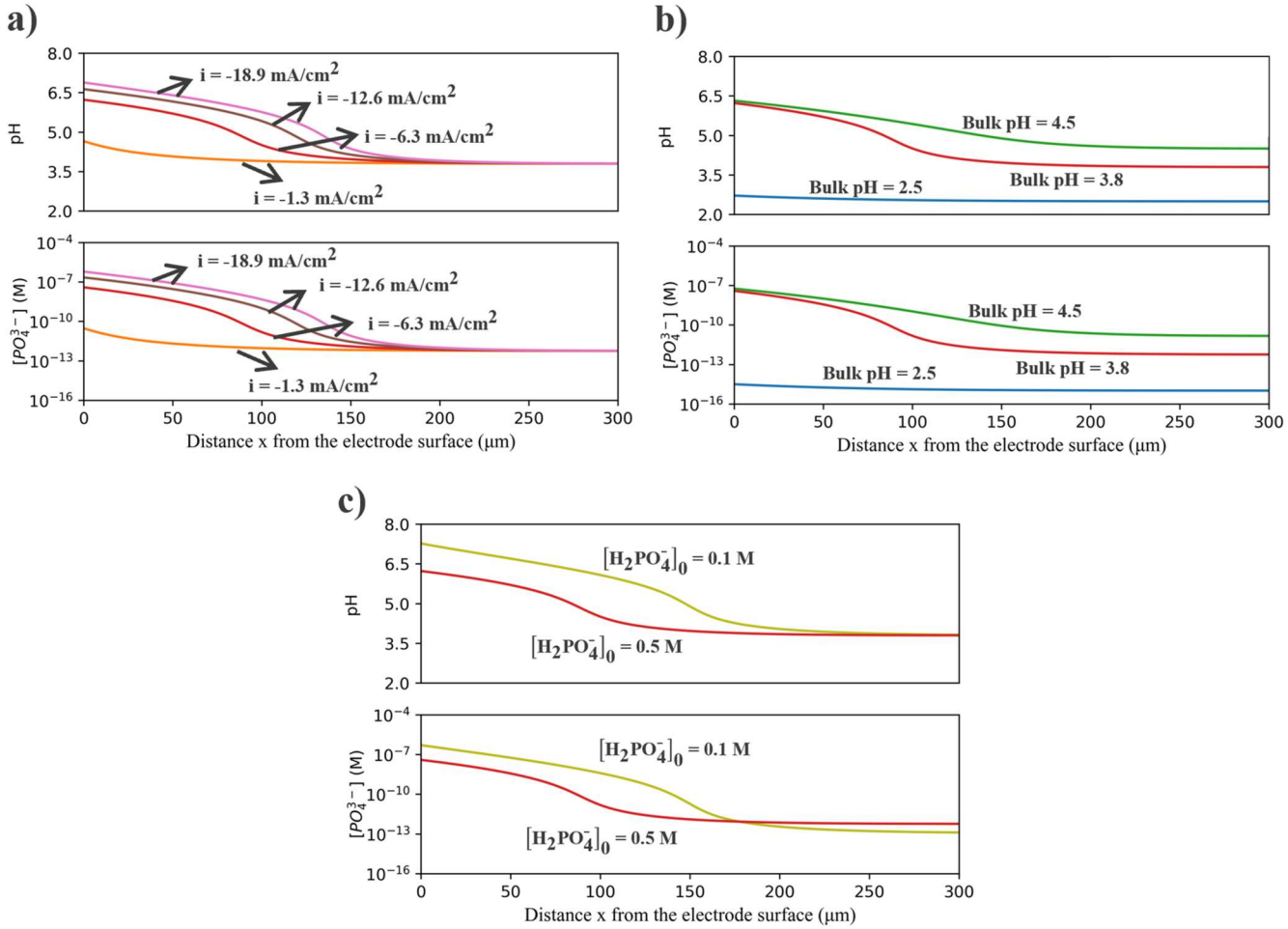

Figure 5. This figure shows (a) a numerical model for the diffusion layer pH and the diffusion layer $[PO_4^{3-}]$ for experiments performed with 4 different current densities (-1.3 mA cm^{-2} (orange), -6.3 mA cm^{-2} (red), -12.6 mA cm^{-2} (brown), and -18.9 mA cm^{-2} (pink)) with solution (bulk pH = 3.8 and $[H_2PO_4^-]_0$ = 0.5 M), (b) a numerical model for the diffusion layer pH and the diffusion layer $[PO_4^{3-}]$ for experiments performed with an $i = -6.3$ mA cm^{-2} with 3 different bulk pH values for the precursor solution (bulk pH = 2.5 (blue), bulk pH = 3.8 (red), bulk pH = 4.5 (green)), and (c) a numerical model for the diffusion layer pH and the diffusion layer $[PO_4^{3-}]$ for experiments performed for experiments performed using solution A and solution C with an $i = -6.3$ mA cm^{-2} ($[H_2PO_4^-]_0$ = 0.5 M (red) and $[H_2PO_4^-]_0$ = 0.1 M (pear green)).

suggesting that the precipitation reaction could be tailored efficiently by $[H_2PO_4^-]_0$. This finding may seem somewhat counterintuitive to what is commonly reasoned in wet chemistry precipitation where a larger concentration of the precursor results in a greater driving force for precipitation. In this ECiD system, however, the diffusion of ions to and from the electrode surface is an additional factor which

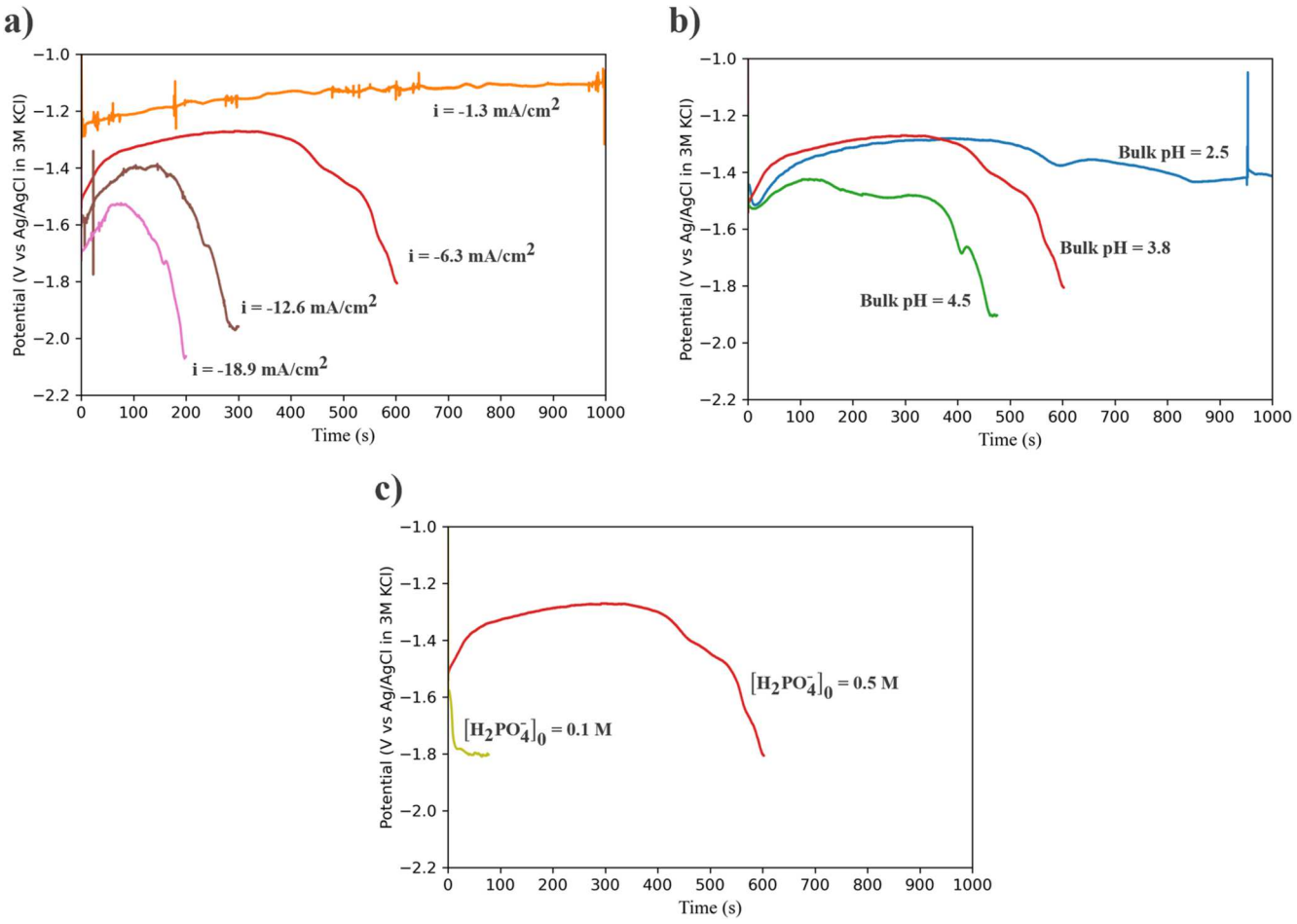

Figure 6. This figure shows (a) the U-t transient for experiments performed with 4 different current densities (-1.3 mA cm^{-2} (orange), -6.3 mA cm^{-2} (red), -12.6 mA cm^{-2} (brown), and -18.9 mA cm^{-2} (pink)) with the solution A (bulk pH = 3.8 and $[H_2PO_4^-]_0 = 0.5$ M), (b) the U-t transient for experiments performed at -6.3 mA cm^{-2} with 3 different bulk pH values for the precursor solution A (bulk pH = 2.5 (blue), bulk pH = 3.8 (red), bulk pH = 4.5 (green)), (c) the U-t transient for experiments performed at $i = -6.3$ mA cm^{-2} with 2 different $[H_2PO_4^-]_0$ values for the precursor solution A ($[H_2PO_4^-]_0 = 0.5$ M (red) and $[H_2PO_4^-]_0 = 0.1$ M (pear green)).

dynamically changes the ratios of species within the near surface environment of the depletion/accumulation layers.

With the model findings as a starting point, experimental investigations of the effect of the applied current density, the bulk pH, and the $[H_2PO_4^-]_0$ were performed. Figure 6 shows the U-t transients for experiments performed with varying current density, bulk pH, and $[H_2PO_4^-]_0$. When the current density is increased from -6.3 mA cm^{-2} to -12.6 mA cm^{-2} and -18.9 mA cm^{-2}, the characteristic features of the transient (as described for Fig. 3f) become increasingly more compressed in time, as seen in Fig. 6a. The positive change in potential and the subsequent negative change as well as the point of maximum coverage occur sooner with an increasing applied cathodic current density. For instance, the point of maximum coverage occurs 300 s earlier with a current density of -12.6 mA cm^{-2} and 400 s earlier with a current density of -18.9 mA cm^{-2} compared to the case for a current density of -6.3 mA cm^{-2}. These findings indicate that the precipitation reaction becomes faster with a larger current density, which is consistent with the predictions of the numerical model. For the lowest current density of -1.3 mA cm^{-2} the potential becomes somewhat less negative but, interestingly, the point of maximum coverage is never reached, even when extending the experiment to 4000 s (see SI, Fig. SI.C6). Indeed, optical inspection and SEM confirm that no deposits are obtained in the center of the samples (Fig. SI.C5-6). For these low current densities, the precipitation occurs only around the edges of the sample. Such edge effects on current distribution cannot be captured by the model.

Figure 6b shows the transients obtained for solution pH between 2.5 and 4.5. When the bulk pH changes from 3.8 (Solution A) to 4.5 (Solution C), the point of maximum coverage is reached 130 s faster (Fig. 6b). The increase in potential and the subsequent decrease occur sooner with a more alkaline bulk pH. These findings indicate that a more alkaline bulk pH results in a faster precipitation rate, as predicted by the numerical model and confirmed by SEM (Fig. S.I. C6). When the bulk pH was lowered to 2.5 (Solution B), the point of maximum coverage is never reached. Similar to the case for low current density, optical inspection and SEM confirm that a closed layer is never obtained for this condition (Fig. SI.C6). The numerical model predicts that for a bulk pH of 2.5 the surface $[PO_4^{3-}]$ is orders of magnitude lower than the solubility limit ($[PO_4^{3-}] = 5.5 \times 10^{-13}$ M) and thus that precipitation is not expected for this condition (Fig. SI.C7). Figure 6c shows the transients obtained for $[H_2PO_4^-]_0$ of 0.5 M and 0.1 M. When $[H_2PO_4^-]_0$ is changed from 0.5 M (Solution A) to 0.1 M (Solution D), the point of maximum coverage is reached 540 s faster. This indicates that the precipitation reaction is significantly faster with a lower $[H_2PO_4^-]_0$, again as predicted by the numerical model and confirmed by SEM (Fig. SI.C5).

The general morphology features of the deposits were similar for the different conditions and resemble those of Figs. 3 and 4 (actual SEM images can be found in figure SI.C5). The specific dimensions of the formed particles were quantified by measuring the height of the hemispherical-like particles and their cavities for those particles that were cleaved in the cross-section SEM. Table II compares all conditions that led to Li_3PO_4 coatings and measured at the point of

Table II. This table shows the maximum island density, average island radius, average cavity radius, and average shell thickness for depositions obtained for reactions using Solution A (bulk pH = 3.8 and $[H_2PO_4^-]_0$ = 0.5 M) and a current density of −18.9 mA cm^{-2}, −12.6 mA cm^{-2}, and −6.3 mA cm^{-2}, depositions obtained for reactions using Solution C (bulk pH = 4.5 and $[H_2PO_4^-]_0$ = 0.5 M) and with i = −6.3 mA cm^{-2}, and depositions obtained for reactions using Solution D (bulk pH = 3.8 and $[H_2PO_4^-]_0$ = 0.1 M) with i = −6.3 mA cm^{-2}. The formula for the maximum island density, the Li_3PO_4 loading, and a discussion of the cavity height measurements with examples and schematics (Figs. SI.C8 and SI.C9) can be found in SI appendix C. The column in the center of the table shows the measurements for the deposition obtained using the solution A with an applied current density of −6.3 mA cm^{-2}. This acts as a point of reference to the other conditions.

	−18.9 mA cm^{-2}	−12.6 mA cm^{-2} Solution A	−6.3 mA cm^{-2}	−6.3 mA cm^{-2} Solution C	−6.3 mA cm^{-2} Solution D
Maximum Island Density (10^6 islands cm^{-2})	2.2	2.1	0.8	3.9	15
Hemisphere height (μm)	3.0 ± 0.4	3.0 ± 0.4	5.0 ± 0.5	2.2 ± 0.5	1.1 ± 0.2
Cavity height(μm)	1.4 ± 0.2	1.6 ± 0.4	1.9 ± 0.3	1.0 ± 0.2	0.5 ± 0.1
Moles of Li_3PO_4 deposited (μmol)	1.5	1.4	2.6	1.1	0.6
Average precipitation rate (nmol s^{-1})	7.3	4.7	4.3	2.4	7.4

maximum coverage (at which point the island density does not increase further, see also point (see discussion of Fig. 3). For the same solution (Solution A), the island density varied only by a factor two with a threefold increase in current density (from 0.8 to 2.2×10^6 islands cm^{-2}). The hemisphere height was found to decrease only slightly (less than factor 2) with an increasing current density (from 5 μm to 3 μm). Note that these samples had threefold difference in deposition time. The height of the cavities seem to have decreased with increasing current density (from 1.9 μm to 1.4 μm), however with the limited statistics and the uncertainty in position of the hemisphere cleavage, we cannot be confident this is a real trend (further discussion in SI.C with examples and explanatory schematics in Figs. SI.C8 and SI.C9).

For the same current density with a varied bulk pH from 3.8 (Solution A) to 4.5 (Solution C), the maximum island density increased fourfold from 0.8×10^6 islands cm^{-2} to 3.9×10^6 islands cm^{-2}. It also shows that the hemisphere and cavity height decreased twofold (from 5 and 1.9 μm for a bulk pH of 3.8, to 2.2 and 1.0 μm for a bulk pH of 4.5, respectively).

Varying $[H_2PO_4^-]_0$ had by far the largest effect, where the maximum island density increased one order of magnitude; from 0.8×10^6 islands cm^{-2} to 1.1×10^7 islands cm^{-2} with $[H_2PO_4^-]_0$ from 0.5 M (Solution A) to 0.1 M (Solution D), respectively. With a lower $[H_2PO_4^-]_0$, the hemisphere height decreased fivefold from 5 μm to 1.1 μm and the cavity height decreased fourfold from 1.9 μm to 0.5 μm. This data seems to indicate that the solution composition affects the hemisphere and cavity height much more significantly than the current density.

The average precipitation rate at the point of maximum coverage was estimated from the difference in hemisphere and cavity volumes (Table II). Note that the actual moles of Li_3PO_4 was overestimated as a dense hemisphere shell was assumed and its porosity was ignored, but it allows a qualitative comparison. Whereas the island density or nucleation was found to be strongly dependent on reaction parameters, the variation in average precipitation rate at the point of maximum coverage is small in comparison (estimates from 2 nmol/s to 7 nmol/s which is negligible considering the broad assumptions). Following our mechanism postulated above, the island density is directly related to the hydrogen bubble density. This suggests that the solutions which gave increased maximum island densities and decreased hemisphere heights (due to smaller cavities), i.e., Solutions C and D, create more and smaller surface adhered H_2 bubbles, which then in turn results in the increased island density and decreased hemisphere heights. Solutions with varying pH and salt concentrations will have different viscosities and surface tension, which is turn affects the kinetics of nucleation and detachment of bubbles and kinetics of the precipitation. Once the Li_3PO_4 is seeded around the H_2 bubble, it grows on average with similar rates for all compositions. As hydrogen is continuously formed, it must escape through the hemispherical shells leading to its porous channel-like morphology.

In the following section, the effect of the addition of ethanol and CTAB as co-solvent and surfactants was experimentally investigated. The co-solvent and additives are expected to affect the solution viscosity and surface tension and in turn the bubble nucleation and size as well as the Li_3PO_4 solubility and precipitation kinetics. Figure 7a shows the morphology obtained at the point of maximum coverage with addition of 15 v/v% ethanol (Solution E). In contrast to the needle-like primary particles and pores arranged around the cavities in the absence of additives (Solution A), a coating comprising of randomly oriented shapeless agglomerates is observed. The secondary particles do not have a center cavity, suggesting the primary particles no longer coalesce around a H_2 bubble when ethanol is added. Note that the primary particles are disordered in nature. The tilted secondary particles appear to be lifted off the surface likely by trapped H_2 gas. As H_2 solubility in ethanol is one order of magnitude greater than that in water (3.5×10^{-3} M in ethanol vs 7.9×10^{-4} M in water[16,17]), a greater extent of H_2 will be present in dissolved form and delay the onset of bubble formation. Furthermore, ethanol lowers the surface tension and thus is expected to better facilitate detachment of bubbles from the surface. Both effects will counter the formation of H_2 bubbles as nucleation centers, whereas pH change still proceeds, leading to random precipitation before bubble nucleation. Figure 7c shows the corresponding U-t transient. The point of maximum coverage was reached 3 times faster when the solvent is 15 v/v% ethanol (Solution E) compared to the case when the solvent was water (Solution A). This is partly explained by the smaller coating thickness but also other factors such as lack of structural pores in the secondary particles (as was the case for samples made with Solution A) are likely to contribute to a faster point of maximum coverage. Another contributing factor may be the less viscous nature and surfactant properties of ethanol, which might affect nucleation and morphology.

Figure 7b shows SEM images of the obtained coating for the ECiD with a solution containing 75 mM CTAB in 15 v/v% ethanol (Solution F). The coating consists of dense, oval secondary particles with no visible porosity inside. The secondary particles are comprised of primary particles noticeably smaller compared to those obtained with the other conditions explored in this work. There is no visible cavity inside the secondary particles similar for the solution with 15 v/v% ethanol only, indicating that also here no H_2 bubbles nucleate before precipitation. This coupled with the observed density of secondary particles suggests that H_2 bubbles don't have a strong presence in the coalescence of secondary particles in this system.

In the presence of CTAB in 15 v/v% ethanol (Solution F) the point of maximum coverage was reached after 300 s (Fig. 7c), twice as fast as when water was the solvent and no additive was present (Solution A), but 100 s slower compared to the solution with a 15 v/v % solvent with no additives (Solution E). This delay before the point of maximum coverage can be explained by the larger and denser secondary particles in the presence of CTAB relative to the case

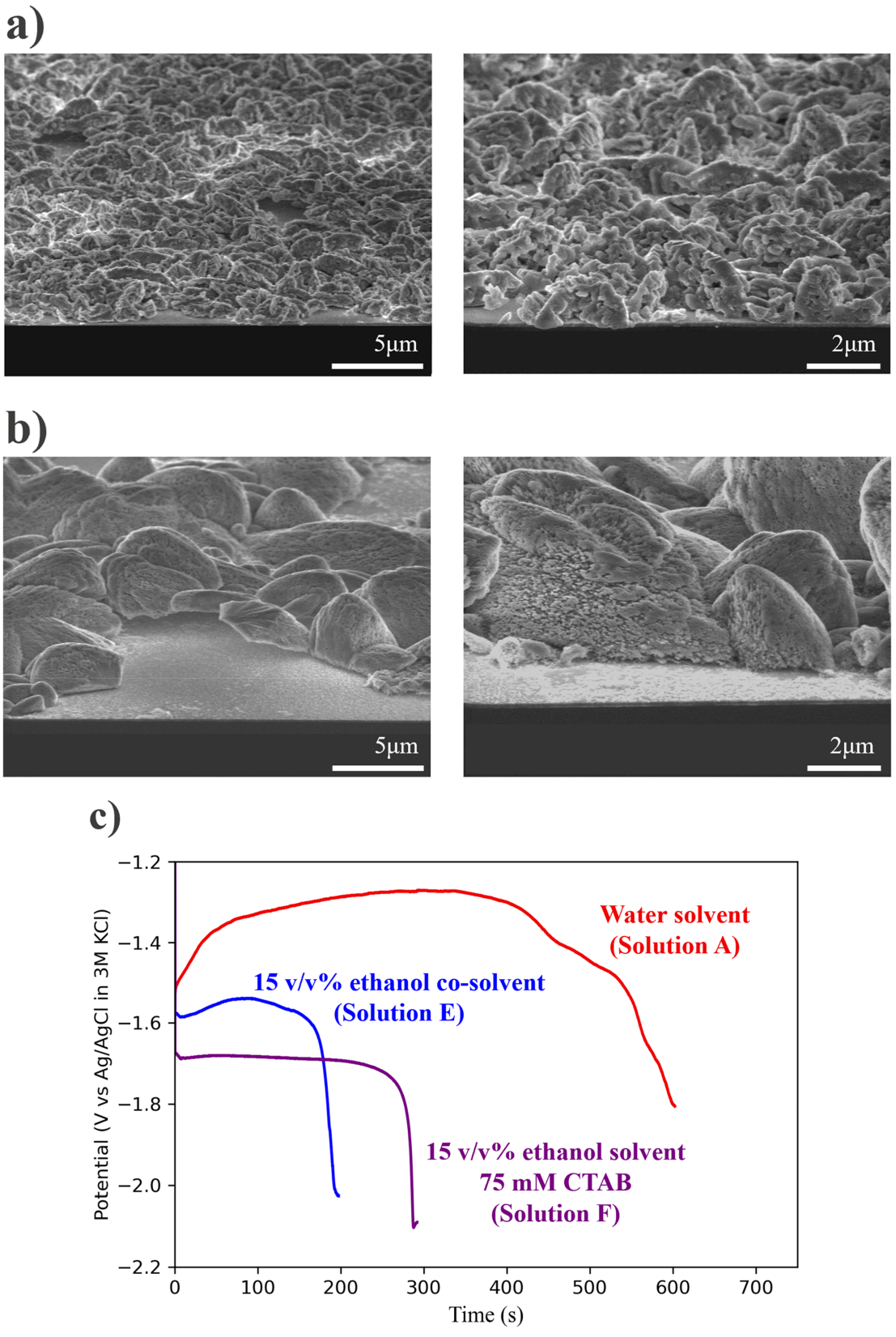

Figure 7. This figure displays (a) two 25° tilted view SEM images of a typical precipitate morphology from a reaction performed with solution E (containing 1.5 M Li_2SO_4 and 0.5 M LiH_2PO_4 in 15 v/v% ethanol with a solution pH of 4.0), (b) two 25° tilted view SEM images of a typical precipitate morphology from a reaction performed with a solution F (containing 1.5 M Li_2SO_4, 0.5 M LiH_2PO_4, and 75 mM CTAB in 15 v/v% ethanol with a solution pH of 4.0), and (c) the U-t transient of three galvanostatic reactions performed with Solution A (containing 1.5 M Li_2SO_4 and 0.5 M LiH_2PO_4 in water with a solution pH of 3.8) (red), solution E (blue) and solution F (purple), all performed with an $i = -6.31$ mA cm^{-2} with Potential, given in V vs Ag/AgCl in 3 M KCl, plotted against time, given in seconds.

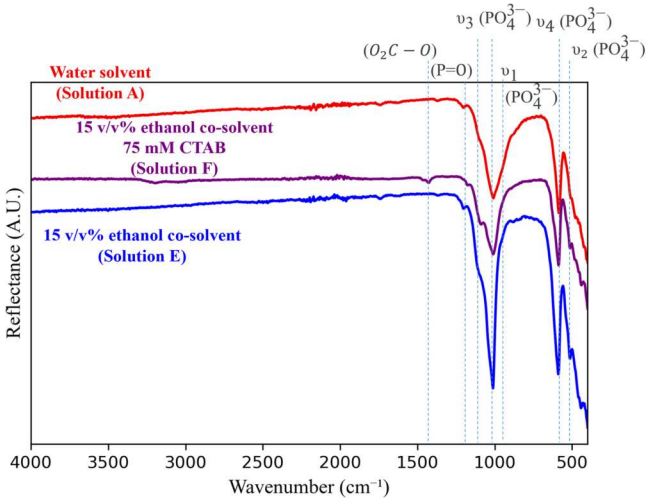

Figure 8. FTIR spectra of a sample prepared using Solution A containing 1.5 M Li_2SO_4 and 0.5 M LiH_2PO_4 in water with a solution pH of 3.8 (red), Solution E containing 1.5 M Li_2SO_4 and 0.5 M LiH_2PO_4 in 15 v/v% ethanol with a solution pH of 4.0 (blue), Solution F containing 1.5 M Li_2SO_4, 0.5 M LiH_2PO_4, and 75 mM CTAB in 15 v/v% ethanol with a solution pH of 4.0 (purple), all performed with a $i = -6.31$ mA cm^{-2} to the point of maximum coverage. Plotted with reflectance, given in arbitrary units (A.U.), against wavenumber, given in cm^{-1}.

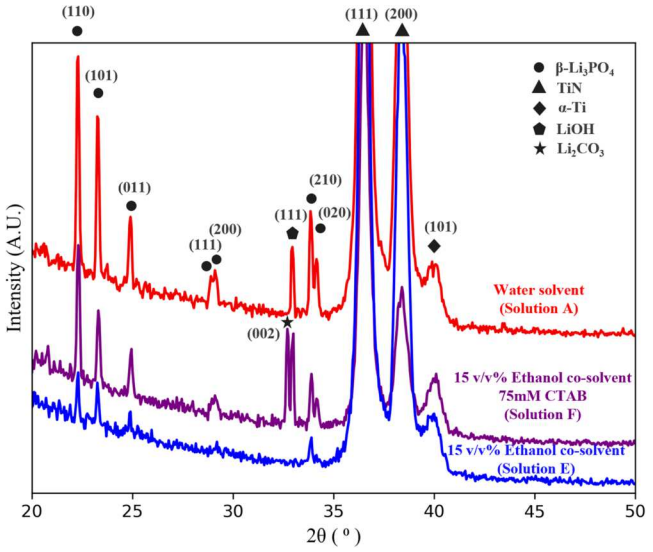

Figure 9. XRD diffractogram of coatings prepared using Solution A containing 1.5 M Li_2SO_4 and 0.5 M LiH_2PO_4 in water with a solution pH of 3.8 (red), Solution E containing 1.5 M Li_2SO_4 and 0.5 M LiH_2PO_4 with 15 v/v% ethanol co-solvent in water with a solution pH of 4.0 (blue), Solution F containing 1.5 M Li_2SO_4, 0.5 M LiH_2PO_4, and 75 mM CTAB with 15 v/v% ethanol co-solvent in water with a solution pH of 4.0 (purple), all performed with an $i = -6.31$ mA cm^{-2} to the point of maximum coverage. Plotted with intensity, given in arbitrary units (A.U.), against 2θ, given in degrees (°). Peaks ascribed to β-Li_3PO_4 are marked with a circle, peaks ascribed to TiN and α-Ti are marked with a triangle and diamond, respectively. The peak ascribed to LiOH is marked with a pentagon, while the peak ascribed to Li_2CO_3 is marked with a star. Note that intensities may be a consequence of the differing coating thicknesses (5.0 μm, 1.6 μm and 2.3 μm, for coatings prepared from Solutions A, E, and F, respectively).

without CTAB, thus maximum coverage is obtained later. Another contributing factor may be the well-known stabilizing effect surfactants have on clusters and intermediates which generally delay nucleation.[18] This effect has been theorized to result in nucleation pathways such as a 2-step nucleation pathway or a pre-nucleation clusters pathway, neither one of which can be excluded in the nucleation mechanism here.

Lastly, chemical characterization was performed on the synthesized coatings. The coatings were analyzed by means of FTIR, ERDA and XRD to examine the phase purity and crystallinity of the deposit and evaluate if CTAB was incorporated in the coating prepared in its presence.

Figure 8 shows FTIR spectra from three samples, namely from Solution A where water was the solvent, from Solution E where the solvent was 15 v/v% ethanol-water, and from Solution F where 75 mM CTAB was added the latter, all performed by galvanostatic deposition with $i = -6.31$ mA cm^{-2} and stopped at the point of maximum coalescence. In FTIR, all three samples displayed four characteristic vibration modes (υ_1- υ_4) of a PO_4^{3-} ion:[6,19] the υ_3 vibrational mode (asymmetric stretching) at 1013 cm^{-1} with a corresponding shoulder, a weak peak at 967 cm^{-1} due to the υ_1 vibrational mode (symmetric stretching), the peaks at 513 cm^{-1} and 589 cm^{-1} arise from the υ_4 and υ_2 vibrational mode (asymmetric bending). The peak around 1200 cm^{-1} can be associated with the P = O stretch and is also seen for all samples. Hence, the coatings are certainly comprised of primarily a phosphate compound. For the coating from Solution F with CTAB, no conclusive evidence for CTAB incorporation was found. The most prominent stretch is that for the asymmetric C-H_2 stretch vibration which is expected at 2925 cm^{-1}. The FTIR does show some small features at 3200 cm^{-1} and 3050 cm^{-1} which were not found for the coatings without CTAB. Note that signatures for interactions with adsorbed water could arise in the range, albeit usually >3200 cm^{-1}, and in this case no peak for free/liquid water was found at 1600 cm^{-1} either. Additionally, minor peaks are found at 1424 cm^{-1} and 1457 cm^{-1} due to O_2C-O stretches and could be the result of Li_2CO_3 impurities formed during storage in air.[20] Very minor peaks at 1370 cm^{-1} and 1770 cm^{-1} are observed for the coatings obtained from Solution A and E but cannot be attributed to possible contamination from the precursors or probable side products.

Atomic ratios were extracted from ERDA for a sample prepared with Solution A (Fig. SI.C12). It showed an O:P ratio of 4.4, and a Li:P ratio of 2.7. In addition, also H atoms were detected H:P of 0.3, bringing the total Li+H content close to the expected ratio of 3. This indicates that the obtained coating has atomic composition of $Li_{2.7}H_{0.3}PO_{4.4}$, or close to Li_3PO_4 as the sample was stored in air.

The XRD diffractogram (Fig. 9) shows crystalline β-Li_3PO_4 was obtained from the three solutions investigated. The peaks at 36.5° and 38.5°, and that at 40.1° are related to the substrate, respectively TiN and Ti films (TiN/Ti/Si).[21,22] The characteristic Li_3PO_4 peaks at 22.3°, 23.3°, 24.9°, 33.9° and 34.2° confirm that the synthesized samples are indeed Li_3PO_4 and the single peak at 29.1° suggests β-Li_3PO_4 was obtained (γ-Li_3PO_4 is expected to have 2 peaks in that region).[19,23] The coatings synthesized from Solutions A and F exhibited a peak at 33.0° attributed to tetragonal LiOH (note that no other peaks are expected for LiOH in this range).[24] The sample synthesized in the CTAB containing solution (Solution F) exhibited an additional peak at 32.8° which could be assigned to Li_2CO_3 impurities.[25] Note that the films had different equivalent thicknesses which may account for difference in peak intensities.

Conclusions

In this study an experimental and numerical investigation was performed on the ECiD of Li_3PO_4. It was shown that throughout the reaction, hemispherical particles progressively form and grow on the electrode surface, eventually coalescing and forming a closed layer. Continued growth leads to layered coating with eventual delamination. The point of maximum coverage before coalescence corresponds to a distinct minimum in the potential transient which is used as endpoint signature for comparative experiments. The individual Li_3PO_4 hemispheres are comprised of a cavity at the center with a shell of needle-shaped grains around it. The cavity is postulated to be

the remanence of surface-adhered H_2 gas bubbles. These gas bubbles act as nucleation and growth sites for the precipitation of lithium phosphate. The slow release of additional formed hydrogen formed under the shell is also likely responsible for directing the growth of the needle-shaped grains. Based on these observations one can imagine that designing an experiment where the bubble size is minimized while the number density is maximized can lead to a significantly increased coating uniformity. The effect of current density, solution pH, $[H_2PO_4^-]_0$, solvent composition, and the presence of additives, more specifically CTAB, was investigated. A higher current density, higher solution pH, and lower $[H_2PO_4^-]_0$ was shown (experimentally and by modelling) to result in a faster precipitation reaction. From the findings it is clear that the reaction parameters play a significant role in the precipitation reaction and that choosing reaction conditions that result in a high surface $[PO_4^{3-}]$ greatly enable the controllability of the coating morphology. The numerical model developed also provides an easy and powerful tool for efficient and informed experimental design. The presence of ethanol as a co-solvent and CTAB as an additive was shown to drastically alter the film morphology. The addition of ethanol as co-solvent resulted in a more disordered deposit. This is due to the increased H_2 solubility and delay in nucleation of H_2 bubbles together with their easier removal as result of ethanol's surfactant properties. The presence of CTAB directed growth towards oval-shaped particles. These results highlight the potential of co-solvents and additives in tuning the coating morphology but also show the increased complexity of the precipitation reaction in the presence of co-solvents and additives. Further in-depth investigations are thus required to determine major trends in their effect on coating morphology.

ORCID

Ali Amir Saleh https://orcid.org/0000-0001-8364-7982
Louis De Taeye https://orcid.org/0000-0002-9891-0007
Sai Gourang Patnaik https://orcid.org/0000-0002-1606-9024
Genis Vanheusden https://orcid.org/0000-0002-9276-0001
Philippe Vereecken https://orcid.org/0000-0003-4115-0075

References

1. S. Xie, Z. Zhou, X. Zhang, and J. Fransaer, "Cathodic deposition of MOF films: mechanism and applications." *Chem. Soc. Rev.*, **52**, 4292 (2023).
2. T. Palanisamy, Y. K. Kao, D. Fritts, and J. T. Maloy, "Electrochemical aspects of the cadmium impregnation process." *J. Electrochem. Soc.*, **127**, 2535 (1980).
3. Y. Zhou and J. A. Switzer, "Growth of cerium(IV) oxide films by the electrochemical generation of base method." *J. Alloys Compd.*, **237**, 1 (1996).
4. K. Ho, "Electrochemical precipitation of nickel hydroxide." *J. Electrochem. Soc.*, **134**, 52C (1987).
5. B. O'Regan, D. T. Schwartz, S. M. Zakeeruddin, and M. Grätzel, "Electrodeposited nanocomposite N-p heterojunctions for solid-state dye-sensitized photovoltaics." *Adv. Mater.*, **12**, 1263 (2000).
6. B. León and J. A. Jansen, *Thin Cal. Phosphate Coatings for Med. Implants* (Springer, New York, NY, USA) 215 (2009).
7. F. Lissandrello, N. Lecis, and L. Magagnin, "Investigating the effect of current density in ultra-fast electrolytic zinc phosphate deposition." *Electrochim. Acta*, **478**, 143840 (2024).
8. S. Von Euw, Y. Wang, and G. Laurent, "Bone mineral: new insights into its chemical composition." *Sci. Rep.*, **9**, 8456 (2019).
9. J. M. Zhang, C. J. Lin, Z. D. Feng, and Z. W. Tian, "Mechanistic studies of electrodeposition for bioceramic coatings of calcium phosphates by an *in situ* pH-microsensor technique." *J. Electroanal. Chem.*, **452**, 235 (1998).
10. H. C. Liu and S. K. Yen, "Electrolytic Li_3PO_4 coating on Pt." *J. of Power Sources*, **159**, 245 (2006).
11. M. C. López, G. F. Ortiz, J. R. González, R. Alcántara, and J. L. Tirado, "Improving the performance of Titania nanotube battery materials by surface modification with lithium phosphate." *ACS Appl. Mater. Interfaces*, **6**, 5669 (2014).
12. N.-W. Li, Y.-X. Yin, C.-P. Yang, and Y.-G. Guo, "An artificial solid electrolyte interphase layer for stable lithium metal anodes." *Adv. Mater.*, **28**, 1853 (2015).
13. M. Emmanuel, P. Papp, G. Schuszter, Á. Deák, L. Janovák, Á. Tóth, and D. Horváth, "Nucleation kinetics of lithium phosphate precipitation." *CrystEngComm*, **24**, 4447 (2022).
14. M. Auinger, I. Katsounaros, J. C. Meier, S. O. Klemm, P. Ulrich Biedermann, A. A. Topalov, M. Rohwerder, and Karl, "Near-surface ion distribution and buffer effects during electrochemical reactions." *Physical Chem. Chemical Physics/PCCP. Physical Chem. Chemical Physics*, **13**, 16384 (2011).
15. D. G. Leaist, "Diffusion in aqueous solutions of sulfuric acid." *Canadian J. of Chem.*, **62**, 1692 (1984).
16. C. Hemme and W. Van Berk, "Hydrogeochemical modeling to identify potential risks of underground hydrogen storage in depleted gas fields." *Applied Sci.*, **8**, 2282 (2018).
17. C. L. Young and P. Pergamon, "for the international union of pure and applied chemistry." *Solubility Data Series*, **5–6**, 97 (1981).
18. S. Xu, D. Cao, Y. Liu, and Y. Wang, "Role of additives in crystal nucleation from solutions: a review." *Cryst. Growth Des.*, **22**, 2001 (2021).
19. A. Bharti, A. Kumar, M. Singh, L. Sharma, V. Chauhan, S. Singh, R. Kumar, and P. D. Sahare, "Synthesis and ML study of Li3PO4 for γ-ray dosimetry." *J. Radioanal. Nucl. Chem.*, **334**, 6497 (2024).
20. B. S. Parimalam, A. D. MacIntosh, R. Kadam, and B. L. Lucht, "Decomposition reactions of anode Solid Electrolyte Interphase (SEI) components with $LiPF_6$." *The J. of Physical Chem. C*, **121**, 22733 (2017).
21. V. Valvoda, R. Kužel, R. Černý, and L. Dobiášová, "Detailed X-ray diffraction study of titanium nitride coatings: some interpretation problems." *Mater. Sci. Eng. A*, **104**, 223 (1988).
22. E. Galvanetto, F. P. Galliano, F. Borgioli, U. Bardi, and A. Lavacchi, "XRD and XPS study on reactive plasma sprayed titanium–titanium nitride coatings." *Thin Solid Films*, **384**, 223 (2001).
23. N. I. P. Ayu, E. Kartini, L. D. Prayogi, M. Faisal, and Supardi, "Crystal structure analysis of Li_3PO_4 powder prepared by wet chemical reaction and solid-state reaction by using X-ray diffraction (XRD)." *Ionics*, **22**, 1051 (2016).
24. Z. Li, S. Ganapathy, Y. Xu, J. R. Heringa, Q. Zhu, W. Chen, and M. Wagemaker, "Understanding the electrochemical formation and decomposition of Li_2O_2 and LiOH with *Operando* X-ray diffraction." *Chem. Mater.*, **29**, 1577 (2017).
25. A. Jain et al., "Commentary: the materials project: a materials genome approach to accelerating materials innovation." *APL Mater.*, [online]**1**, 011002(https://next-gen.materialsproject.org/materials/mp-3054?formula=Li2CO3) (2013).